ARCHIVE OF MECHANICAL ENGINEERING

DOI: 10.24425/ame.2026.12696 Early Access; pp. 1–32

Ali Caglar SONMEZ [1], Jifu GUAN [2]

Heuristic multi-objective control and state estimation algorithm for a semi-active suspension

Received 4 June 2026, **Revised** 4 October 2026, **Accepted** 17 October 2026, **Published online** 19 November 2026

Keywords: semi-active suspension, multi-objective control, state observer, skyhook, ground-hook

This paper proposes a heuristic multi-objective control algorithm for semi-active suspension systems in road vehicles, where the competing objectives are arbitrated by supervisory switching rather than by Pareto-based optimization. Although significant progress has been made in suspension control, a comprehensive strategy that maintains both ride comfort and handling performance across varying road excitation frequencies remains limited. Building on the mixed skyhook-acceleration driven damping (SH-ADD) framework, we integrate velocity-based ground-hook (VBGH) and acceleration-based ground-hook (ABGH) methods into a high-level adaptive controller. The first contribution transfers the band-partitioning principle of mixed SH-ADD to handling-oriented control, reducing tire load variation in both low and high-frequency domains. The second contribution is to design a multi-objective controller that dynamically switches between comfort-oriented and handling-oriented modes in response to vehicle speed, steering input, and operating conditions, such as tire pressure and cabin load. To address practical sensing challenges, we introduce a real-time state estimation algorithm that uses frequency-domain integration of vertical acceleration signals. Simulation results in a joint Simulink–CarSim environment demonstrate significant improvements in ride comfort, handling stability, and path tracking compared with conventional approaches.

1. Introduction

Suspension systems largely determine a vehicle's ride comfort and handling, but passive suspensions are limited by the trade-off between spring rate and damping: high damping improves the response near resonance but degrades it at higher

✉ Ali Caglar SONMEZ, e-mail: kgs24@mails.tsinghua.edu.cn

[1]School of Vehicle and Mobility, Tsinghua University, Beijing, China.

[2]Department of Mechanical Engineering, Beijing Institute of Technology, Beijing, China.

© 2026. The Author(s). This is an open-access article distributed under the terms of the Creative Commons Attribution (CC-BY 4.0, https://creativecommons.org/licenses/by/4.0/), which permits use, distribution, and reproduction in any medium, provided that the author and source are cited.

frequencies, and low damping does the opposite. Semi-active suspensions adjust the damping in real time through a controllable damper, and offer performance comparable to active suspensions at lower energy consumption and cost [1]. This paper concerns the control algorithm rather than the actuator.

Semi-active control strategies include heuristic [2], fuzzy [3], model predictive [4], and neural-network-based [5] approaches. Model-based strategies such as H_∞ and model predictive control (MPC) can deliver optimal performance, but depend on an accurate plant model and substantial online computation. Heuristic laws trade this optimality for model independence and a very low computational load, which is why they remain common in production semi-active suspensions and are the focus of this work. The best known are the comfort-oriented skyhook (SH) control, which emulates a damper attached to an inertial reference in the sky [6], and acceleration-driven damping (ADD), derived from optimal control theory [7].

Savaresi et al. [8] showed that SH and ADD are each near-optimal only within one frequency band, SH below a cross-over frequency near the body resonance and ADD above it, and the mixed SH-ADD algorithm switches between the two according to an estimate of the excitation frequency. Both target comfort, i.e., the sprung-mass acceleration. Handling is addressed by ground-hook control, which emulates a damper between the wheel and the ground to reduce the dynamic tire load [9]; it is effective around the wheel-hop resonance but worse than a passive suspension at low frequencies. Kopylov et al. [10] proposed acceleration-based ground-hook (ABGH), which replaces its velocity terms with acceleration terms and is effective at low frequencies. In this paper, the classical ground-hook is referred to as a velocity-based ground-hook (VBGH), only to make its symmetry with ABGH explicit. Whereas mixed SH-ADD covers the whole excitation band for comfort, the handling-oriented laws have so far remained band-limited. Both mixed algorithms, moreover, depend on a cross-over frequency that shifts with cabin load and tire stiffness, but is normally fixed at design time.

All of these laws require the absolute and relative velocities of the sprung and unsprung masses, which are difficult to measure on a vehicle, and state observers such as Kalman filters are therefore widely used. Model-based estimation was adopted for the semi-active suspension of a light commercial vehicle [11], an observer-based sliding-mode controller accounting for actuator dynamics was proposed in [12], and estimated states were used in a road-frequency adaptive scheme in [13]. Such observers depend on a plant model and are sensitive to its inaccuracies. Frequency-domain integration of measured accelerations avoids the model, but in [14] it was performed offline, for signal evaluation.

Strategies that pursue ride comfort and road holding simultaneously fall into two conceptually distinct families. They are separated not by how the two objectives are weighted, but by whether an explicit joint cost function combining them is minimized at all.

The first family is optimization-based multi-objective control, in which the competing requirements are written into a single mathematical criterion, and the

controller is obtained by optimizing it. Two branches of this family are common. In the first, the objectives are scalarized into a weighted cost that is then minimized by a model-based synthesis method, such as linear quadratic regulation, mixed H_2/H_∞ design as applied to semi-active suspensions in [15], or model predictive control [4]; each choice of weights yields one controller, and sweeping the weights sweeps out the attainable trade-off. In the second, the objectives are retained as a vector criterion, and the whole trade-off set is computed explicitly by multi-objective evolutionary optimization. The relevant notion of optimality is then Pareto optimality: a candidate solution is Pareto-optimal, or non-dominated, when no other feasible candidate improves one objective without degrading at least one of the others, and the set of such solutions forms the Pareto front, which bounds the best attainable comfort–handling compromise of a given architecture. This approach has been applied to the design and tuning of semi-active and controlled suspensions in [16], in [17], and in [18]. Heuristic and evolutionary multi-objective optimization is not confined to suspension design: it has likewise been applied to piezoelectric energy harvesters for tire pressure monitoring [19], to time-cost compromised workflow scheduling [20], to heterogeneous fleet routing [21], and to image encryption [22]. What both branches share is a formal optimality claim with respect to a stated cost, obtained at the price of a model of the plant and of a non-negligible computational effort.

Optimization-based and robust control methods have also been applied to other vehicle subsystems, including active variable geometry suspension [23], electric power steering [24], longitudinal driving strategies for autonomous vehicles [25], mechanical systems subject to actuator saturation [26], electromagnetic braking [27], and energy management in electric vehicles [28]. Related modeling work on vehicle noise and on layered structures includes the attenuation of turbocharger inlet sound propagation [29] and the layerwise analysis of poroelastic composite plates [30].

The second family is heuristic supervisory arbitration. Here, no joint criterion is formed: single-objective control laws are designed separately, each addressing one requirement, and a higher-level logic decides how they are combined during operation. The best-known example is the hybrid skyhook–ground-hook (SH-GH) controller, in which a constant weighting factor blends the skyhook and ground-hook damping forces into a single command [31], an approach also assessed experimentally on a quarter-car test rig [32]. Because the weighting factor is fixed, the resulting balance is set at design time and does not change with the driving condition. Adaptive SH-GH schemes schedule the blending weight online from the measured excitation or from the driving state, as in the adaptive hybrid strategy of [33], the driving-behavior-based strategy of [34], and the full-body control strategy validated on a supercar in [35]. Mode selection has also been posed as a multi-objective optimization problem for a switching hydraulically interconnected suspension [36], and weighted multi-objective methods, such as entropy-weighted TOPSIS combined with evolutionary optimization, have been used to arbitrate be-

tween competing suspension objectives [37]; such formulations also admit criteria beyond lateral acceleration, such as roll and pitch behavior. Arbitration of this kind carries no optimality certificate, but it inherits the model independence and the very low computational footprint of the underlying heuristic laws.

The distinction is therefore one of optimality guarantee rather than of adaptivity: the first family produces a solution that is optimal, or non-dominated, with respect to an explicitly stated criterion, whereas the second selects among predesigned control laws by rule and makes no such claim. The algorithm proposed in this paper belongs to the second family. Accordingly, the term *multi-objective* is used throughout this paper in the sense of multi-objective *control*, that is, a supervisory layer arbitrating in real time between separately designed comfort- and handling-oriented controllers, which amounts to conditional switching between single-objective controllers. It is not used in the sense of multi-objective *optimization*: no joint cost function combining comfort and handling is minimized, and no Pareto front is computed. This point is developed further in Sec. 6, and a formal Pareto-based treatment is identified as future work.

Finally, a high-level architecture is required that integrates two low-level controllers, one for comfort (mixed SH-ADD) and one for handling (mixed VBGH-ABGH), and decides between them in real time according to the driving condition rather than through a fixed compromise. In this paper, the decision is based on the vehicle's calculated lateral acceleration, and the architecture is evaluated in joint CarSim–Simulink simulations of a double lane change and a racetrack lap.

The specific contributions of this paper are the following.

1. A mixed VBGH-ABGH control law is proposed, which applies velocity-based and acceleration-based ground-hook damping in their respective effective bands and reduces the tire load variation in both the low- and high-frequency domains. The band-partitioning principle itself is inherited from mixed SH-ADD [8]; the contribution is its transfer to the handling domain.
2. An adaptive cross-over frequency update method is developed. Both cross-over frequencies are read from offline calibration maps using the sprung mass and tire stiffness estimated at each engine start, so that the switching boundaries follow the cabin load and tire pressure of each trip.
3. A real-time state estimation method based on the fast Fourier transform (FFT) is introduced. Frequency-domain integration of vertical acceleration is reformulated to run causally on a sliding window, providing the absolute and relative velocities required by the heuristic laws without a plant model, an observer, or additional displacement sensors.
4. A supervisory multi-objective control architecture is proposed that arbitrates between the two objectives instead of blending them. Each objective is assigned to a controller that is effective across the whole excitation band and designed for that objective alone (mixed SH-ADD for comfort, mixed VBGH-ABGH for handling). The architecture thus adapts along two axes:

the excitation frequency inside each low-level controller, and the driving condition in the supervisor through the lateral acceleration. Fixed-weight hybrid SH-GH schemes adapt along neither axis, and adaptive SH-GH schemes along the second only.

Sec. 2 recalls the background algorithms and states the problem. Sec. 3 develops the mixed VBGH-ABGH algorithm, Sec. 4 the adaptive cross-over frequency update, Sec. 5 the FFT-based state estimator, and Sec. 6 the supervisory controller and its full-vehicle verification. Sec. 7 concludes the paper.

2. Background algorithms and problem statement

2.1. Quarter-car semi-active suspension model

A single-wheel, 2-degree-of-freedom model, widely referred to as the quarter-car model, can be used to describe the semi-active suspension vertical motion [38]:

$$\begin{aligned} m_b\ddot{z}_b &= -c(\dot{z}_b - \dot{z}_w) - k_b(z_b - z_w - \Delta_s) - m_b g, \\ m_w\ddot{z}_w &= c(\dot{z}_b - \dot{z}_w) + k_b(z_b - z_w - \Delta_s), \\ &\quad - k_w(z_w - z_r - \Delta_w) - m_w g, \\ \dot{c}_s &= -\beta c_s + \beta c_{\text{in}} \quad [c_{\min} \le c_{\text{in}} \le c_{\max}], \end{aligned} \tag{1}$$

where z_b, z_w, and z_r represent the positions of the body, the wheel, and the road profile along the vertical axis, respectively; m_b and m_w are the sprung and unsprung masses, respectively. k_w and k_b denote the stiffness of the tire and the suspension, respectively. Δ_s and Δ_w represent the lengths of the spring and the tire under static load. As long as the tire-road contact is guaranteed, i.e., $z_r - z_w < \Delta_w$, the tire can be modeled as a linear spring. The first-order dynamic relationship governing the actual damping coefficient c_{in} captures the modulation delay in the damping command, where β is the modulation bandwidth of the semi-active shock absorber. Unless otherwise mentioned, the following parameters are used in this paper: $m_b = 400\,\text{kg}$, $m_w = 50\,\text{kg}$, $k_b = 25\,\text{kN/m}$, $k_w = 200\,\text{kN/m}$, $\beta = 30$, $c_{nominal} = 1.5\,\text{kNs/m}$, $c_{min} = 0.3\,\text{kNs/m}$, $c_{max} = 4\,\text{kNs/m}$.

2.2. Mixed SH-ADD control

The skyhook concept couples the sprung mass to an ideal damper anchored to an inertial reference in the sky. A widely used two-state approximation of it is [38]:

$$c_{\text{in}} = \begin{cases} c_{\max}, & \text{if } \dot{z}_b(\dot{z}_b - \dot{z}_w) \ge 0 \\ c_{\min}, & \text{if } \dot{z}_b(\dot{z}_b - \dot{z}_w) < 0 \end{cases}. \tag{2}$$

Developed by solving a finite-time optimal control problem using the Maximum Principle of Pontryagin when there is no road preview information and the

objective is to minimize vertical body acceleration [7]. The ADD control law can be written in the form of:

$$c_{\text{in}} = \begin{cases} c_{\max}, & \text{if } \ddot{z}_b(\dot{z}_b - \dot{z}_w) \geq 0 \\ c_{\min}, & \text{if } \ddot{z}_b(\dot{z}_b - \dot{z}_w) < 0 \end{cases}. \tag{3}$$

Approximate frequency response analysis revealed notable complementarities between the SH and ADD algorithms. As shown in Figure 1, a characteristic frequency, referred to as the SH-ADD cross-over frequency, was identified just beyond the first resonance frequency where two curves intersect. This frequency delineates the regions where each algorithm performs optimally: SH is more effective below the cross-over point, while ADD outperforms SH beyond it. Developed over this finding, the mixed SH-ADD algorithm dynamically switches between SH and ADD based on the instantaneous excitation conditions, thereby making full use of the advantages of each algorithm [8]. The mixed SH-ADD control algorithm can be written as:

$$c_{\text{in}} = \begin{cases} c_{\max}, & \text{if either} \\ & \quad \dot{z}_b(\dot{z}_b - \dot{z}_w) \geq 0 \wedge f_{\text{exc}} < \alpha, \\ & \quad \ddot{z}_b(\dot{z}_b - \dot{z}_w) \geq 0 \wedge f_{\text{exc}} \geq \alpha \\ c_{\min}, & \text{if either} \\ & \quad \dot{z}_b(\dot{z}_b - \dot{z}_w) < 0 \wedge f_{\text{exc}} < \alpha, \\ & \quad \ddot{z}_b(\dot{z}_b - \dot{z}_w) < 0 \wedge f_{\text{exc}} \geq \alpha \end{cases}, \tag{4}$$

where α is the SH-ADD cross-over frequency, and f_{exc} is the frequency of the road excitation z_r. In Figure 1, it is observed that mixed SH-ADD offers an improved comfort through the whole working frequency between 0-20 Hz. Mixed SH-ADD algorithm adopts the following indirect estimation logic to judge if excitation frequency is above or below the cross-over frequency [8]. It requires only the sprung-mass acceleration and velocity, which are already needed by the control law itself, and is adopted in this paper for the same purpose:

$$f_{\text{excitation}} \begin{cases} > \alpha, & \text{if } \ddot{z}_b^2 - \alpha^2 \dot{z}_b^2 > 0 \\ < \alpha, & \text{otherwise} \end{cases}. \tag{5}$$

Both the mathematical derivation of this condition and its verification under broadband excitation are provided by Savaresi et al. [8]. The mixed SH-ADD configuration is excellent at filtering sprung-mass vibration acceleration, but at the cost of increased non-sprung mass vibration, which affects dynamic tire load and may cause the very risky phenomenon, wheel hop, if the following condition occurs [38]:

$$(z_w - z_r) \geq \frac{m_b g + m_w g}{k_w}. \tag{6}$$

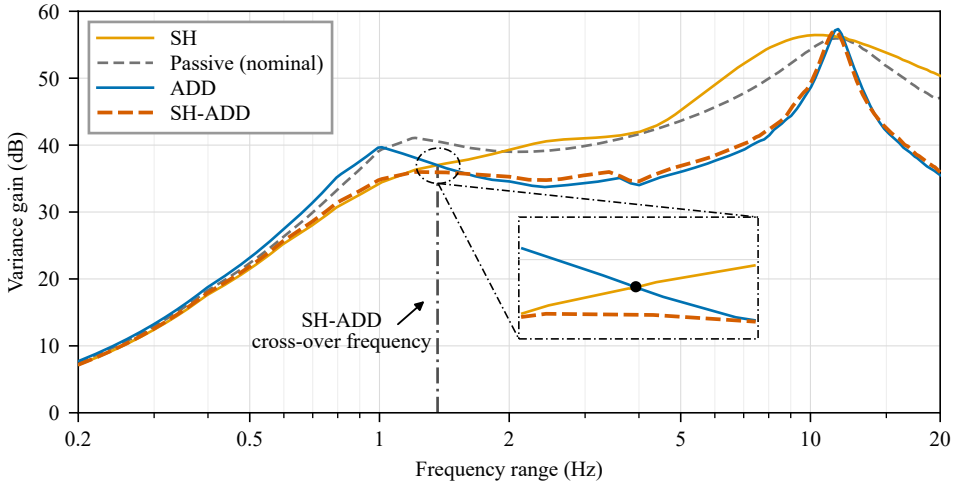


Fig. 1. Frequency response from road disturbance to the body acceleration

Two assumptions underlie (1). The suspension spring is taken as linear over its working range, which is standard for ride and handling analysis in the frequency band of interest, and the tire is represented as a linear spring, which holds only while contact with the road is maintained. Equation (6) marks the boundary of this second assumption: when the tire deflection reaches the static value, the tire force falls to zero, and beyond that point the tire can no longer pull the wheel towards the road. The linear model would then over-predict the restoring force, so the quarter-car model is used here only up to that boundary, and (6) serves to detect the limit rather than to describe the behavior past it. The quarter-car model is used in Sec. 2 to Sec. 5, where the excitation levels keep the tire in contact. The full-vehicle results of Sec. 6 are obtained in CarSim, whose tire model represents loss of contact directly, so those results do not rely on the linear tire assumption.

2.3. VBGH and ABGH algorithms

VBGH, the classical ground-hook law introduced in Sec. 1, is a heuristic approximation of the ideal ground-hook damper and can be written as [9]:

$$c_{in} = \begin{cases} c_{\max}, & \text{if } \dot{z}_w(\dot{z}_b - \dot{z}_w) \leq 0 \\ c_{\min}, & \text{if } \dot{z}_w(\dot{z}_b - \dot{z}_w) > 0 \end{cases}. \tag{7}$$

Initially developed to overcome the practical problems in velocity measurement, ABGH replaces the velocity terms of VBGH with acceleration terms. Using the acceleration-based heuristic algorithm, the controller is able to detect the anti-phase oscillations as effectively as the VBGH controller [10]. The ABGH control law can

be written as:

$$c_{in} = \begin{cases} c_{\max}, & \text{if } \ddot{z}_w(\ddot{z}_b - \ddot{z}_w) \leq 0 \\ c_{\min}, & \text{if } \ddot{z}_w(\ddot{z}_b - \ddot{z}_w) > 0 \end{cases}. \tag{8}$$

The handling performance of the two algorithms, VBGH and ABGH, is compared using an approximate frequency response analysis (FR). Reducing the dynamic tire load variations improves the handling performance. Following the frequency-domain system identification framework of [39], the variance gain from road excitation to tire deflection, FR_{td}, can be written as:

$$FR_{\text{td}}(w_i) = \sqrt{\frac{\frac{1}{T}\int_0^T (z_{w_i}(t) - z_{r_i}(t))^2\, dt}{\frac{1}{T}\int_0^T (z_{r_i}(t))^2\, dt}} \quad i \in \mathbb{N}. \tag{9}$$

From the results provided in Figure 2, it can be observed that the VBGH control algorithm minimizes tire deflection variations around the second resonance frequency (also called unsprung mass resonance frequency) and performs poorly at lower frequencies. On the contrary, the ABGH algorithm performs worse than the VBGH algorithm around the unsprung mass resonance frequency and performs effectively in lower frequency ranges, including the sprung mass resonance frequency.

2.4. Problem statement

Based on the provided framework, following questions arising are tried to be answered within this paper:

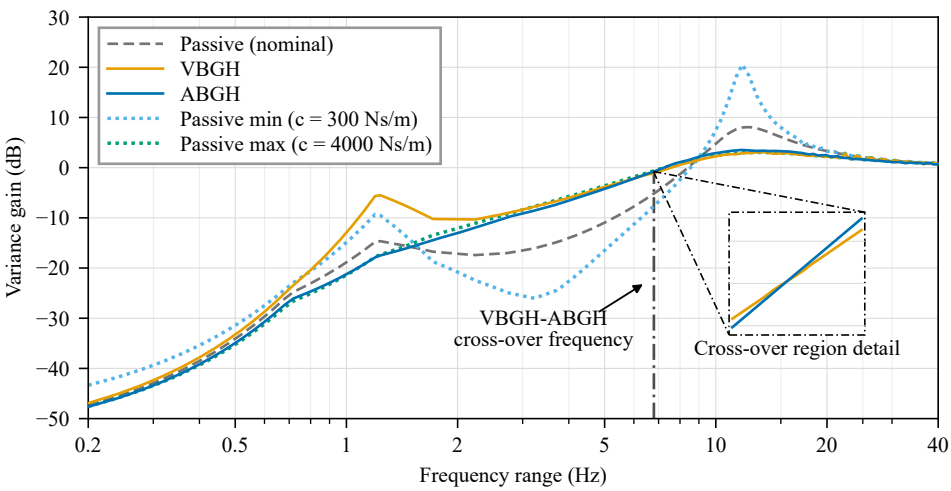


Fig. 2. Frequency response from road disturbance to tire deflection. The VBGH and ABGH curves intersect at the handling cross-over frequency Ω, which defines the switching boundary of the mixed VBGH-ABGH algorithm

1. Can an adaptive, multi-objective control algorithm be developed that (i) behaves as VBGH below the handling cross-over frequency and as ABGH above it, and (ii) switches between comfort- and handling-oriented modes in response to driving conditions, road excitation, and vehicle states?
2. Can the cross-over frequency be updated adaptively in real time to reflect changes in tire pressure and cabin load?
3. Can a practical, real-time state variable estimation algorithm be implemented without requiring complex sensors?

3. Mixed VBGH-ABGH algorithm

The VBGH-ABGH cross-over frequency Ω, which will also be named the handling cross-over frequency later in this study, is defined as the frequency at which the variance gain curves of the VBGH and ABGH algorithms intersect in Figure 2, that is, the frequency above which VBGH yields the lower tire deflection and below which ABGH does. It is obtained numerically from the approximate frequency response analysis, and for the parameters used in this study, it falls at approximately 7 Hz, close to the midpoint between the sprung and unsprung mass resonance frequencies.

Getting inspiration from the comfort-oriented mixed SH-ADD algorithm, a handling-oriented mixed algorithm that makes use of two distinct control algorithms at their best-performing frequency ranges is proposed. Similar to the comfort-oriented mixed SH-ADD algorithm, this handling-oriented algorithm is very simple to implement yet highly effective. Interestingly, VBGH and ABGH algorithms have very similar formulations; the only difference is replacing velocity terms with acceleration.

It is worth stating explicitly what is, and what is not, claimed as novel here. The principle of partitioning the excitation spectrum and assigning a dedicated control law to each band is not introduced by this paper: it is due to the mixed SH-ADD algorithm [8], and no conceptual novelty is claimed for frequency-based switching as such. The novelty, therefore, lies in transferring the band-partitioning idea to the handling domain and in making it operable in real time, not in the switching concept itself:

$$c_{\text{in}} = \begin{cases} c_{\max}, & \text{if either} \\ & \ddot{z}_w(\ddot{z}_w - \ddot{z}_b) \geq 0 \wedge f_{\text{exc}} < \Omega, \\ & \dot{z}_w(\dot{z}_w - \dot{z}_b) \geq 0 \wedge f_{\text{exc}} \geq \Omega \\ c_{\min}, & \text{if either} \\ & \ddot{z}_w(\ddot{z}_w - \ddot{z}_b) < 0 \wedge f_{\text{exc}} < \Omega, \\ & \dot{z}_w(\dot{z}_w - \dot{z}_b) < 0 \wedge f_{\text{exc}} \geq \Omega \end{cases} . \tag{10}$$

The same indirect logic used for the comfort branch in (5) supplies the frequency information required by (10), with the handling cross-over frequency Ω replacing the comfort cross-over frequency α:

$$f_{\text{excitation}} \begin{cases} > \Omega, & \text{if } \ddot{z}_b^2 - \Omega^2 \dot{z}_b^2 > 0 \\ < \Omega, & \text{otherwise} \end{cases}, \tag{11}$$

so that no additional sensor or estimator is introduced by the mixed VBGH-ABGH algorithm.

3.1. Mixed VBGH-ABGH algorithm verification

The approximate frequency response simulation for the mixed VBGH-ABGH algorithm is presented in Figure 3. Figure 3 shows that the mixed VBGH-ABGH algorithm has optimal performance in both low and high frequency regions. It behaves almost identically with ABGH in the low frequency region and VBGH around the second resonant frequency. In order to further validate the mixed VBGH-ABGH algorithm, the following analysis will be held in the time domain: pure tone sinusoidal excitation with two distinct frequencies, and broadband random road signal. Firstly, two distinct pure-tone sinusoidal signals $A\sin(\omega_i t)$ are used as road excitation frequencies, where $\omega_1 = 1.5$ Hz (sprung mass resonance frequency) and $\omega_2 = 10$ Hz (unsprung mass resonance frequency). Tire deflection responses are presented in Figure 4. The amplitude of the sinusoidal signals, $A = 0.05$ meters, is set for both cases.

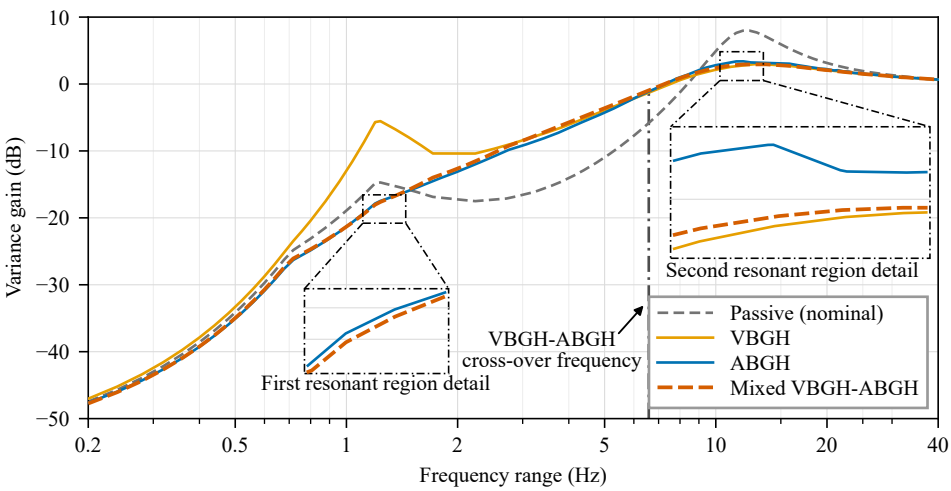


Fig. 3. Frequency response of the mixed VBGH-ABGH algorithm. The mixed law follows ABGH below Ω and VBGH above it, attaining the lower tire deflection of the two across the whole excitation range

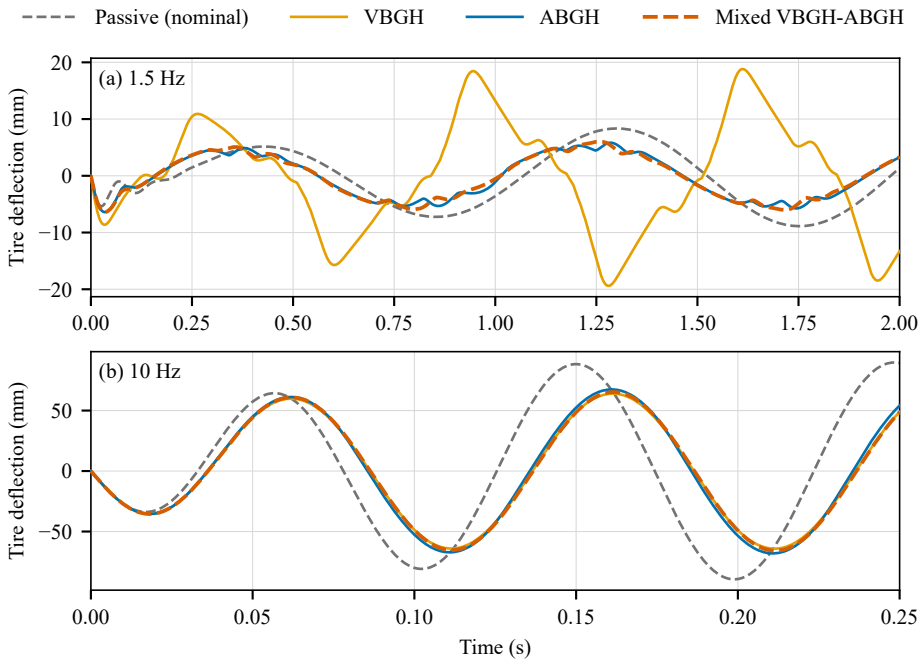


Fig. 4. Tire deflection time domain response to sinusoidal disturbances at (a) 1.5 Hz and (b) 10 Hz. The mixed algorithm matches ABGH at the low frequency and VBGH at the wheel-hop frequency, confirming the branch selection

From Figure 4(a), it can be observed that when the road excitation frequency is 1.5 Hz, the VBGH algorithm performs worse than the nominal passive suspension. In contrast, the ABGH algorithm demonstrates highly effective performance at this low frequency, outperforming both the VBGH and passive configurations, as expected. Notably, the performance of the mixed VBGH-ABGH algorithm is nearly equivalent to that of the standalone ABGH algorithm. Furthermore, the proposed mixed VBGH-ABGH control reduces the tire deflection relative to the passive damper by 38% and 31%, in terms of the Root Mean Square (RMS) and Maximum Absolute Error (MaxAE) metrics, respectively.

Figure 4(b) shows that under 10 Hz excitation, VBGH is the best-performing control algorithm, and the performance of mixed VBGH-ABGH is almost identical to it. Even though the 31% improvement of the mixed VBGH-ABGH algorithm over the ABGH algorithm seems not too significant at first sight. However, this percentage corresponds to a 2.6 mm improvement in tire deflection RMS, which is a valuable improvement since this is the unsprung mass resonant frequency.

For the stochastic simulation, ISO-8608 Class D random road input is used, and the vehicle speed is 60 km/h. The time-domain response of the tire deformation, along with RMS and MaxAE values, is shown in Figure 5 and Table 1.

Table 1. Dynamic tire deflection response to ISO-8608 Class D road profile. RMS: root mean square; MaxAE: maximum absolute error; percentages are reductions relative to the passive suspension

Performance index	Passive (nominal)	Mixed VBGH-ABGH	VBGH	ABGH
RMS (mm)	3.73	2.44 (↓34.7%)	2.84 (↓23.8%)	3.43 (↓8.0%)
MaxAE (mm)	12.58	8.33 (↓33.7%)	9.69 (↓22.9%)	11.72 (↓6.8%)

The promising performance of the mixed VBGH-ABGH controller can be easily seen. The mixed VBGH-ABGH controller outperforms both VBGH and ABGH controllers. The RMS improvement of mixed VBGH-ABGH is 34.7% over the passive case.

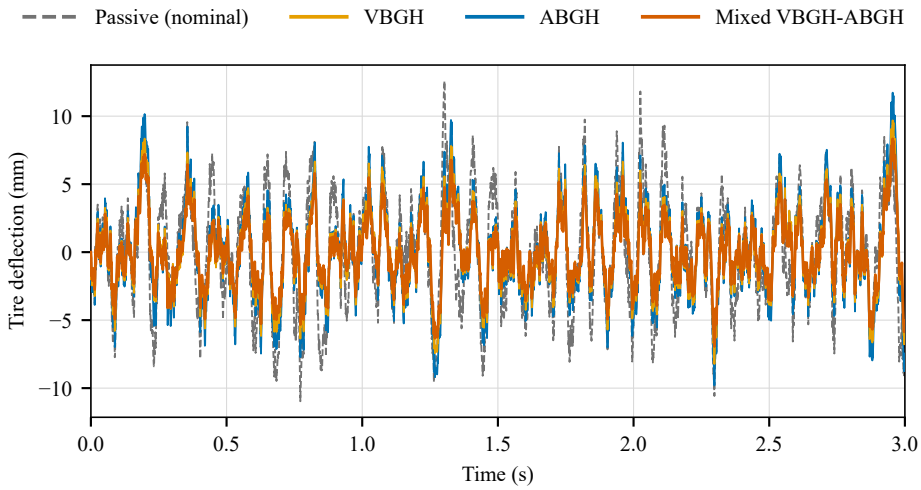


Fig. 5. Tire deflection under the ISO 8608 Class D random road profile at 60 km/h

4. Adaptive cross-over frequency update method

Tire pressure and vehicle load variations affect comfort-oriented and handling-oriented cross-over frequencies, and this paper proposes an adaptive selection method as follows; Firstly, the offline calibration process will be carried out. While tire pressure $k_{w,j}$ is kept the same, the sprung mass $m_{s,i}$ value will be changed with increments from low to high:

$$\begin{aligned} m_{s,i} &= [m_{s,1}, m_{s,2}, \ldots, m_{s,N}], \quad \text{where } i = 1, \ldots, N, \\ k_{w,j} &= [k_{w,1}, k_{w,2}, \ldots, k_{w,N}], \quad \text{where } j = 1, \ldots, N. \end{aligned} \tag{12}$$

Frequency response analysis for comfort-oriented SH and ADD algorithms, as provided in Figure 1, and handling-oriented VBGH and ABGH algorithms,

as provided in Figure 2, will be repeated at each increment. The corresponding comfort and handling cross-over frequencies will be recorded.

Subsequently, the tire stiffness parameter will be incremented by one step, and the sprung mass values will again be incrementally varied from low to high. This process will be repeated until the cross-over frequencies corresponding to all combinations are obtained.

By doing so, two heuristic 2D calibration matrices of size $N \times N$ will be constructed, one for comfort and one for handling, as shown in equations (13) and (14):

$$\alpha(k_w, m_s) = \begin{bmatrix} \alpha_{1,1} & \cdots & \alpha_{1,N} \\ \vdots & \ddots & \vdots \\ \alpha_{N,1} & \cdots & \alpha_{N,N} \end{bmatrix}, \tag{13}$$

$$\Omega(k_w, m_s) = \begin{bmatrix} \Omega_{1,1} & \cdots & \Omega_{1,N} \\ \vdots & \ddots & \vdots \\ \Omega_{N,1} & \cdots & \Omega_{N,N} \end{bmatrix}. \tag{14}$$

Secondly, obtaining the input signals k_w and m_s required for the adaptive algorithm is possible without the need to install additional sensors, as most commercial vehicles are already equipped with tire pressure sensors. The tire stiffness can be estimated using pneumatic tire pressure data, based on the relationship provided by the Rhyne equation [40]:

$$k_w = 0.00028P\sqrt{D} \times W + 3.45, \tag{15}$$

where P is the inflation pressure in pascals (Pa), W is the tread width, and D is the overall diameter of the wheel in meters. The sprung mass value m_s can be obtained by solving the dynamic equation of the sprung mass inversely and assuming $\ddot{z}_s = (\dot{z}_s - \dot{z}_w) = (z_s - z_w) = 0$ while the vehicle is stationary. Rearranging the equation, m_s can be expressed as a function of the static suspension deflection Δ_s:

$$m_s = \frac{k_b \Delta_s}{g}. \tag{16}$$

Since Eq. (16) holds only in static equilibrium, it is evaluated once, at engine start, while the vehicle is stationary, and the resulting m_s is held for the rest of the key cycle.

Lastly, a calibration update mechanism should be constructed within the control algorithm so that the corresponding comfort and handling cross-over frequencies are fed to the control algorithm based on the current value of the (k_w, m_s) pair. This update need not be performed continuously, since the (k_w, m_s) pair varies only slowly; a calibration refresh at each engine key cycle already captures the

dominant trip-to-trip changes in cabin load and cold-tire pressure. The refresh is triggered by the engine-start signal, which is directly available on the vehicle CAN bus, so no additional detection logic is required. Intermediate (k_w, m_s) pairs that do not fall on the calibration grid are resolved by bilinear interpolation between the four neighboring grid entries, and pairs outside the calibrated range are clamped to the nearest grid boundary. The schematic representation of the adaptive cross-over frequency update mechanism is shown in Figure 6

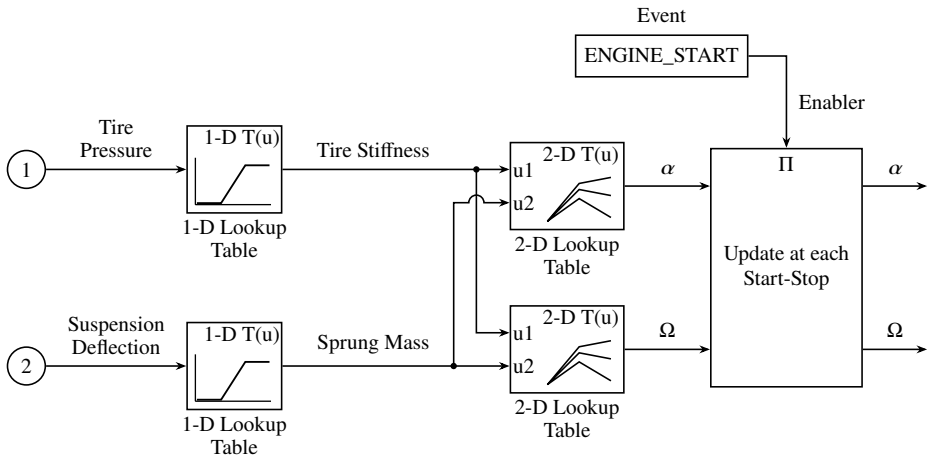


Fig. 6. Schematic diagram of the adaptive cross-over frequency update method

Figure 7 shows the calibrated 2-D map of the comfort and handling oriented cross-over frequency variation with respect to tire stiffness and sprung mass. From Figure 7(a) it can be seen that comfort cross-over frequency increases as tire stiffness increases and decreases as sprung mass increases. While it is dependent on both variables, the influence of the sprung mass variation is more significant than the influence of the tire stiffness. This observation is consistent with the theoretical expectation since the comfort performance indicator is the sprung mass acceleration, which is affected significantly by the value of the sprung mass. From Figure 7(b), it is observed that despite comfort cross-over frequency, handling cross-over frequency has a proportional relationship with both sprung mass and tire stiffness . While it is dependent on both variables, the influence of the tire stiffness is more significant than the influence of the sprung mass. It is worth noting that this relationship is the exact inverse of the relationship in the comfort-frequency case. Since the maps are consulted once per key cycle, tire heating and intermediate load changes are not captured.

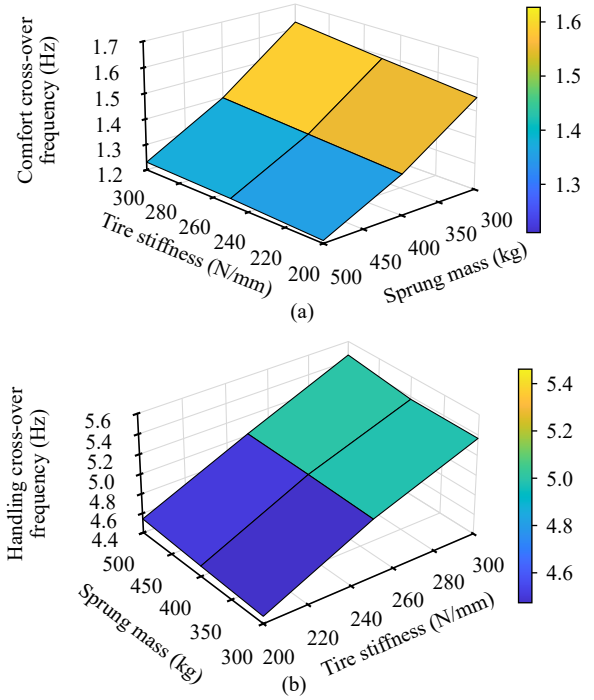


Fig. 7. 2-D maps for comfort and handling cross-over frequency calibration. The comfort cross-over rises with tire stiffness and falls with sprung mass, whereas the handling cross-over rises with both

5. FFT based state variable estimation method

State estimation is a key obstacle to the engineering realization of the SH, ADD, VBGH, and ABGH algorithms, which all require the absolute and relative velocities of the sprung and unsprung masses, quantities that are difficult to measure directly. The method proposed here requires only two accelerometers mounted on the sprung and unsprung masses; its realization and simulation-based verification are given below.

Using the Fourier transform, any acceleration signal $a(t)$ can be represented as:

$$a(t) = Ae^{j\omega t}, \tag{17}$$

where ω denotes the angular frequency of the signal, A is the amplitude, and j is the imaginary unit. Integration of Eq. 17 yields a velocity signal of:

$$v(t) = \int_0^t Ae^{j\omega\tau}\, d\tau = \frac{A}{j\omega} e^{j\omega t} = Ve^{j\omega t}. \tag{18}$$

Here, $v(t)$ is the velocity Fourier component at frequency ω and $V = A/j\omega$ is its coefficient. A second frequency-domain integration would likewise yield the displacement ($X = -A/\omega^2$), but the controller of Section 6 requires only the velocities $\dot{z}_b$ and $\dot{z}_w$, so the displacement is not computed here.

No high-pass filtering of the acceleration spectrum is required. A constant accelerometer bias is represented entirely by the zero-frequency component of the transform, and that component is necessarily discarded during the integration because $1/j\omega$ is undefined at $\omega = 0$. The estimate is therefore immune to sensor bias by construction: biases of 0.5, 2 and 50 m/s^2 were found to change the estimated velocity by less than 10^{-16} m/s. Removing further low-frequency components, as is customary when acceleration signals are integrated, would only discard genuine signal content, since 43% of the variance of the sprung-mass velocity lies below 1 Hz; the cost of doing so is quantified in Sec. 5.2.

After frequency-domain integration, an inverse FFT (IFFT) recovers the time-domain velocity. For real-time operation the algorithm runs over a sliding buffer of N samples; let $\dot{z}_k[n]$, $n = 0, \ldots, N-1$, denote the estimated velocity in the k^{th} window, where $\dot{z}$ is either $\dot{z}_b$ or $\dot{z}_w$ depending on the sensor. The window advances every ΔN samples; with starting index $t_k = k\,\Delta N$, the windowed acceleration is:

$$a_k[n] = a(t_k + n), \quad n = 0, 1, \ldots, N-1.$$

Applying FFT, integration in the frequency domain, and inverse FFT yields the raw velocity estimate for the window:

$$\dot{z}_k[n] = \text{IFFT}\left(\frac{A_k[\omega]}{j\omega}\right), \quad n = 0, 1, \ldots, N-1.$$

Because each window is processed independently, the integration ignores the cumulative nature of the velocity across windows, causing discontinuities at window boundaries; an offset-correction step removes them.

Let $\dot{z}_{k-1}[\Delta N]$ be the velocity value at the shifting index of the previous window. The corrected velocity array is then obtained by:

$$\dot{z}_k^{\text{corr}}[n] = \dot{z}_k[n] + \dot{z}_{k-1}[\Delta N], \quad n = 0, 1, \ldots, N-1. \tag{19}$$

This ensures that the first point in the new window aligns with the last point of the previous window, satisfying:

$$\dot{z}_k^{\text{corr}}[0] = \dot{z}_k[0] + \dot{z}_{k-1}[\Delta N] = \dot{z}_{k-1}[\Delta N].$$

This offset correction approach maintains signal continuity across successive sliding windows and is critical for enabling accurate, real-time state variable estimation in the semi-active suspension control algorithm. Because the zero-frequency component of the velocity spectrum is set to zero in every window, the integrated velocity carries no constant or slowly varying bias that could accumulate, and the

estimate cannot drift over long driving periods. Based on the theory described above, the process flow of the proposed algorithm is illustrated in Figure 8. The parameters used, selected as described in Sec. 5.1 and Sec. 5.2, are shown in Table 2.

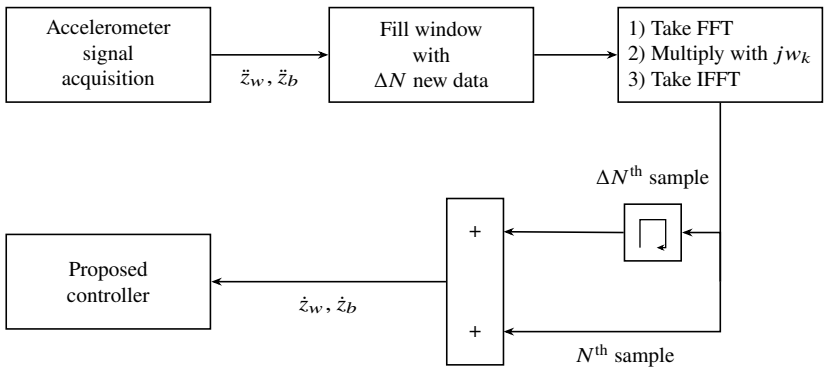


Fig. 8. Schematic representation of the proposed online state estimation algorithm

Table 2. Parameters used for online FFT-based state variable estimator test

Parameters	**Value**
z_{road}	ISO 8608 (D class)
$v_{\text{longitudinal}}$	50 km/h
t_{init}	4 s
f_{accel}	1024 Hz
f_{est}	128 Hz
N	4096 samples
ΔN	8 samples

Where z_{road} represents the road grade, $v_{\text{longitudinal}}$ is the vehicle speed, $t_{\text{initialization}}$ is the initialization time, $f_{\text{accelerometer}}$ is the acceleration sampling frequency, and $f_{\text{estimation}}$ is the estimation frequency of the speed, i.e., how often the algorithm obtains the speed. N is the number of data points sampled in the acceleration window, and ΔN is the increment of the number of points sampled in the sliding window. Simulation results are presented in Figure 9.

5.1. Estimator design and parameter selection

The estimator has three parameters: the sampling frequency f_s, the window length N, and the window advance ΔN. Each should be selected based on separate requirements and the sensitivity analysis proposed in this study.

The sampling frequency is not a free parameter. It is the rate at which the vertical acceleration signal is sampled, and is defined by the accelerometer sensor used. For an industry-level accelerometer signal $f_s = 1024$ Hz can be assumed.

The window length N is the number of acceleration samples held in the sliding buffer. A window of N samples covers a time span $T = N/f_s$, and the discrete Fourier transform of that window produces spectral lines spaced by:

$$\Delta f = \frac{f_s}{N} = \frac{1}{T}, \tag{20}$$

where Δf is the frequency resolution of the estimator. Two components closer together than Δf cannot be separated, and no component slower than Δf can be represented at all.

N is therefore set by the lowest frequency that must be resolved. The sprung-mass velocity is dominated by the body resonance, so it is this resonance that governs the choice. For the quarter-car parameters listed in Sec. 2.1, the undamped natural frequency f_n of the sprung mass and its damping ratio ζ at the nominal damping are:

$$f_n = \frac{1}{2\pi}\sqrt{\frac{k_b}{m_b}} = 1.26 \text{ Hz}, \qquad \zeta = \frac{c_{nominal}}{2\sqrt{k_b m_b}} = 0.24. \tag{21}$$

The resonance is not a single line but a peak whose half-power bandwidth is $2\zeta f_n = 0.60$ Hz. At least two spectral lines must fall inside this bandwidth for the peak to be resolved, which requires $\Delta f \leq 0.30$ Hz, and by (20) this means $N \geq 3431$. The smallest power of 2 satisfying this is $N = 4096$, giving $\Delta f = 0.25$ Hz and a window of $T = 4$ s. A power of two is used so that a radix-2 transform can be applied.

The window advance ΔN is the number of new samples taken in between successive updates. It does not affect accuracy, and is selected in Sec. 5.2 from the refresh rate and the computational load.

Table 3 shows how the estimation error varies with N, measured on two independent 15 s segments of an ISO-8608 class D road profile and reported as the worse of the two. The error falls steadily as the window lengthens, so N is a trade-off rather than an optimum. A longer window gives finer resolution, but costs more computation and memory, needs a proportionally longer start-up before the first estimate is available, and relies more heavily on the excitation staying steady across the window, which is less true during transient events. Below $N = 2048$ fewer than two spectral lines fall inside the body resonance, and the error rises above 20% of the signal RMS. $N = 4096$ is therefore the smallest window that meets the resolution requirement.

5.2. Computational cost and refresh interval

One update requires a forward and an inverse N-point FFT together with N complex divisions, that is $2 \cdot 5N \log_2 N + 6N = 5.16 \times 10^5$ floating-point operations

Table 3. Sensitivity of the estimation accuracy to the window length N (f_s = 1024 Hz, ΔN = 16)

N	T (s)	Δf (Hz)	Buffer (kB)	RMSE (m/s)	RMSE / signal RMS
512	0.50	2.000	2.0	0.01266	65.9%
1024	1.00	1.000	4.0	0.00677	35.3%
2048	2.00	0.500	8.0	0.00399	20.8%
3072	3.00	0.333	12.0	0.00259	13.5%
4096	4.00	0.250	16.0	0.00174	9.1%
6144	6.00	0.167	24.0	0.00128	6.7%
8192	8.00	0.125	32.0	0.00087	4.5%

for $N = 4096$, and the sliding buffer occupies 16 kB in single precision. The window advance ΔN sets the refresh interval $\Delta N / f_s$ and, inversely, the sustained computational load; it has no effect on accuracy. Table 4 reports this trade-off, with the measured execution time of a single update being 0.12 ms in MATLAB on a laptop processor (Intel Core i5-13500H).

$\Delta N = 8$ is selected, giving a refresh interval of 7.8 ms, which satisfies a sub-10 ms requirement for control actuation, at a sustained load of 66 MFLOP/s. Halving ΔN again would double the load for no accuracy benefit, while $\Delta N = 16$ would exceed 10 ms. Between updates, the previous estimate is held. Here, real-time means that each update is completed well within the refresh interval. An automotive control unit may run the damper control task at a shorter period, for example, 1 ms, in which case each estimate is reused over about eight task cycles. The 7.8 ms interval is, however, short compared with the damper time constant $1/\beta \approx 33$ ms of Eq. (1).

Because only the center sample of the inverse transform is used, each update is a fixed linear combination of the N buffered samples. It can therefore be computed, with identical output, as an inner product with an N-point kernel obtained once offline from the FFT integration. This requires $2N = 8192$ floating-point operations per update, 63 times fewer than the FFT form, or 1.05 MFLOP/s per channel at $\Delta N = 8$. The assumed target is one core of a 32-bit automotive microcontroller with a single-precision floating-point unit at about 300 MHz, such as the AURIX TC3xx family. Assuming one to two clock cycles per multiply-accumulate, one update takes 14–27 μs, and the eight channels of a four-corner vehicle, one per sprung- and unsprung-mass accelerometer, occupy less than 3% of the core. The memory required is a 16 kB buffer per channel and one 16 kB constant kernel shared by all channels. For comparison, a linear four-state quarter-car Kalman filter with a full covariance update requires about 0.5 MFLOP/s per corner at 1024 Hz, and a 14-state full-vehicle filter about 21 MFLOP/s, so the cost of the proposed estimator is of the same order.

Table 4. Refresh interval and computational load against the window advance ΔN ($N = 4096$, $f_s = 1024$ Hz)

ΔN	Refresh (Hz)	Interval (ms)	MFLOP/s	RMSE (m/s)	RMSE / signal RMS
4	256	3.91	132.1	0.00174	9.1%
8	128	7.81	66.1	0.00174	9.1%
16	64	15.62	33.0	0.00174	9.1%
32	32	31.25	16.5	0.00175	9.1%
64	16	62.50	8.3	0.00176	9.2%
128	8	125.00	4.1	0.00177	9.2%

5.3. Robustness to measurement noise and sensor faults

The estimator was evaluated under four classes of sensor imperfection: additive white noise, a stuck sensor, 16-bit quantization over a $\pm 2g$ range, and a constant bias. Each case was applied to the same two 15 s segments used above.

White noise represents the broadband noise floor of the sensor, and was applied as a zero-mean Gaussian signal added to the acceleration. The estimator is largely resistant to this imperfection, because the $1/\omega$ weighting of the frequency-domain integration acts as a low-pass filter: at 0.01 m/s^2 RMS the error is unchanged, and at 0.1 m/s^2 RMS, which is 40% of the RMS of the acceleration signal itself, it grows only by a factor of 1.4.

A stuck sensor represents a frozen output, in which the last valid sample is held for the duration of the fault, and was applied by holding the acceleration constant for a fixed interval. This is the most damaging of the four cases, because the frozen samples enter the transform as genuine low-frequency content: a fault lasting 0.05 s increases the error by a factor of 2.4, and one lasting 0.2 s by a factor of 6.2. A production implementation, therefore, requires a signal-plausibility monitor to detect a frozen or disconnected accelerometer and to hold the last valid estimate until the signal recovers; no such monitor is included here.

Quantization represents the finite resolution of the digital sensor output, and was applied by rounding the acceleration to a 16-bit grid spanning $\pm 2g$, a step of 5.99×10^{-4} m/s^2. It has no measurable effect since the rounded value is orders of magnitude smaller than the RMS of the body acceleration signal.

A constant bias represents a fixed offset in the sensor output and was applied by adding a constant to the acceleration. The estimate is unaffected by it, and the error is identical to the fault-free case for offsets of 0.5 and 2 m/s^2 alike. This is not a matter of degree: a constant is represented entirely by the zero-frequency component of the transform, and that component is necessarily discarded during the integration, as described in Sec. 5. The algorithm, therefore, handles sensor bias exactly rather than approximately. Table 5 summarizes these results.

As shown in Figure 9, the simulation results indicate that the estimation performance of the proposed algorithm is consistent with the theoretical data derived

Table 5. Robustness of the state estimator to sensor imperfections ($N = 4096$, $\Delta N = 8$; acceleration signal RMS = 0.2531 m/s^2)

Condition	RMSE (m/s)	MaxAE (m/s)	Ratio to clean
Clean	0.00174	0.00556	1.00
White noise σ = 0.01 m/s^2	0.00173	0.00554	1.00
White noise σ = 0.05 m/s^2	0.00210	0.00772	1.21
White noise σ = 0.10 m/s^2	0.00242	0.00663	1.39
Stuck sensor, 0.05 s	0.00409	0.01384	2.35
Stuck sensor, 0.2 s	0.01082	0.03374	6.22
16-bit quantization ($\pm 2g$)	0.00174	0.00556	1.00
Constant bias 0.5 m/s^2	0.00174	0.00556	1.00
Constant bias 2.0 m/s^2	0.00174	0.00556	1.00

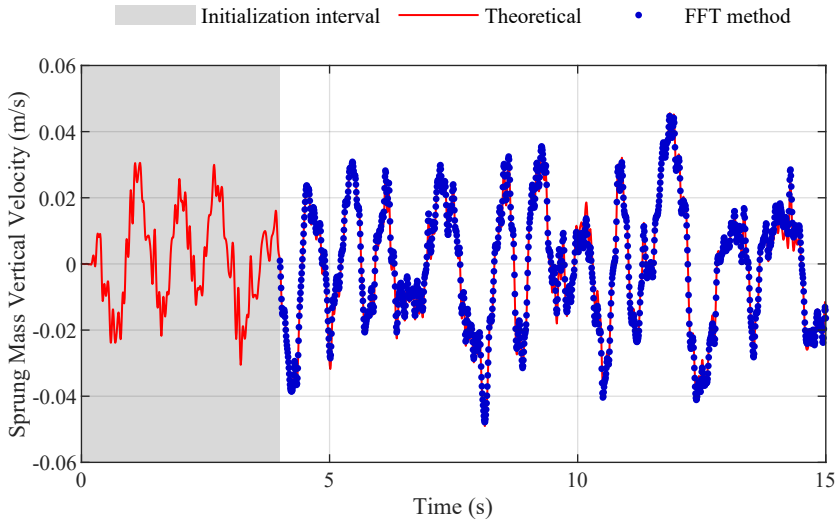


Fig. 9. Simulated vs. theoretical values for real time state variable estimation

from the quarter-car model given in Eq. 1. The sprung-mass velocity is estimated with a MaxAE of 0.0056 m/s.

6. Multi-objective control algorithm

A higher-level architecture is now proposed that switches between the mixed SH-ADD and mixed VBGH-ABGH controllers according to the driver's instantaneous need for comfort or handling. It should be clarified that the term *multi-objective* is used here in the sense of multi-objective *control*: a supervisory layer that arbitrates in real time between two separately designed single-objective controllers according to the prevailing driving condition. It does not denote multi-objective

optimization in the Pareto sense: no joint cost function combining comfort and handling is minimized, and no Pareto front is computed. Each low-level controller continues to optimize its own single objective (sprung-mass acceleration for comfort, dynamic tire load for handling), and the supervisor selects which objective is prioritized rather than trading them off along an optimal front. A formal Pareto-based multi-objective optimization is a worthwhile but separate undertaking and is identified as future work.

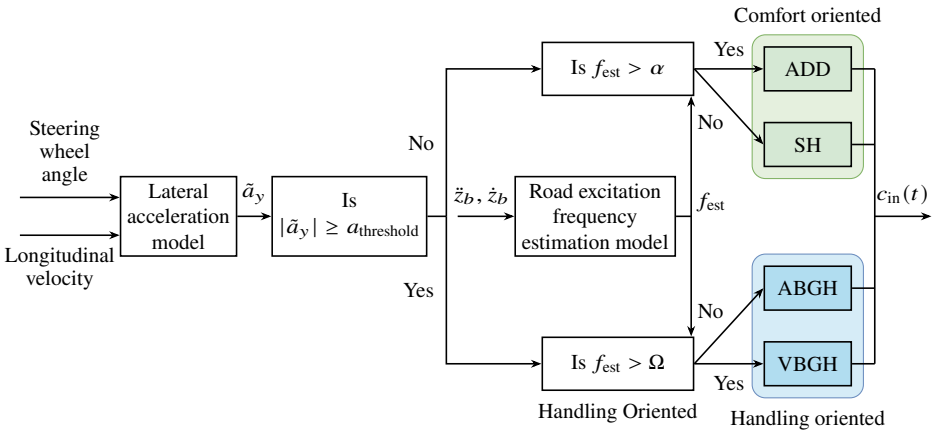


Fig. 10. Schematic representation of the multi-objective control algorithm

The switching is driven by a simple modeled lateral acceleration computed online from longitudinal velocity and steering-wheel angle. A high lateral acceleration unbalances the wheel load distribution and makes the wheels prone to slip, creating a safety risk; accordingly, when the modeled lateral acceleration exceeds a threshold, the supervisor selects the handling objective, and otherwise the comfort objective, as shown in Figure 10.

This supervisory switching law is expressed as:

$$c_{\text{in}} = \begin{cases} c_{\text{VBGH-ABGH}}, & \text{if } |\tilde{a}_y| \geq a_{\text{threshold}} \\ c_{\text{SH-ADD}}, & \text{if } |\tilde{a}_y| < a_{\text{threshold}} \end{cases}. \tag{22}$$

Here, $c_{\text{SH-ADD}}$ denotes the damping determined by the SH-ADD logic, and $c_{\text{VBGH-ABGH}}$ denotes the damping determined by the VBGH-ABGH logic. $\tilde{a}_y$ represents the estimated lateral acceleration, and $a_{\text{threshold}}$ denotes the lateral acceleration threshold. In this study $a_{\text{threshold}} = 2.5$ m/s^2 is used. The value was selected empirically from a series of CarSim maneuvers, low enough for the supervisor to identify a genuine handling maneuver, yet high enough that the mode does not alternate during ordinary straight-line driving. It is therefore a tuning parameter rather than a physical limit: lowering it gives a more handling-oriented, sporty character, and raising it a more comfort-oriented one.

In its present form, the supervisory law in (22) is a hard (bang-bang) threshold: when the estimated lateral acceleration dwells near $a_{\text{threshold}}$, small fluctuations can cause the controller to switch repeatedly between the comfort and handling modes. The effect of such switching on the damper is bounded, because both low-level laws command only $c_{\min}$ or $c_{\max}$; a change of mode therefore produces no larger damping step than either law produces by itself, and the first-order damper dynamics in (1) smooth it further. Introducing a hysteresis dead-band (separate on/off thresholds) or a smooth blending buffer around the switching boundary, together with a sweep of $a_{\text{threshold}}$, is identified as a future improvement.

Lateral acceleration can be obtained using an IMU sensor. However, due to implementation costs and direct measurement delays, this study proposes using a lateral static model based on vehicle speed and steering angle [35]. The estimation formula is as follows:

$$\tilde{a}_y = \frac{\delta V^2}{L + V^2 K_{us}}, \tag{23}$$

where L is the wheelbase, V is the vehicle speed, and δ is the steering angle, K_{us} is the under-steer gradient, which can be determined based on the specific vehicle model [41]. In the implementation, $\tilde{a}_y$ is high-pass filtered to remove offset. Figure 11 compares it with the CarSim lateral acceleration on the racetrack: the model leads during transients but underestimates sustained values, as it omits tire saturation and load transfer. It nevertheless remains above $a_{\text{threshold}}$ for most of the cornering phase.

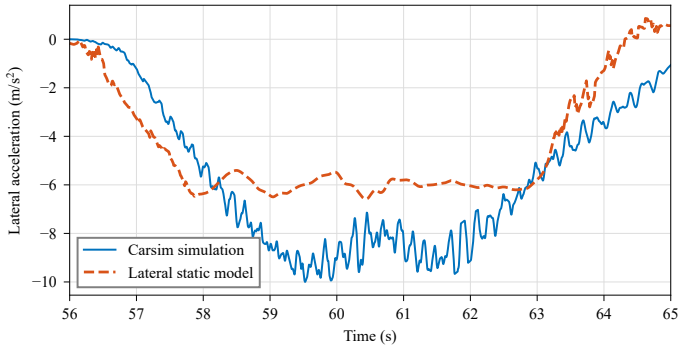


Fig. 11. Modeled and CarSim lateral acceleration during a cornering phase of the racetrack test

6.1. Simulation verification of the proposed multi-objective controller

Since the supervisor switches rather than blends, each low-level controller has been benchmarked against its constituent laws in Figure 1 and in Figures 2–5 and Table 1; the full-vehicle tests below therefore compare the complete architecture

with the passive suspension. The high-level controller is verified through joint CarSim–Simulink simulations of a D-Class sedan whose four suspensions are controlled independently; the co-simulation setup is shown in Figure 12. The vehicle is the CarSim 2019.1 D-Class Sedan (sprung mass 1370 kg, wheelbase 2866 mm, independent suspension at all four wheels, 215/55 R17 tires), whose nonlinear passive dampers are replaced by linear dampers with the coefficient set by the controller. CarSim runs at 2000 Hz. Each corner has its own low-level controllers, fed by the sensors at that corner, and the four damping forces are imported into CarSim; the supervisor, driven by the single estimate $\tilde{a}_y$, selects the same mode for all four corners. The DLC is driven at about 50 km/h. On the racetrack, the CarSim closed-loop driver follows the race line with a 0.4 s single-point preview and an aggressive speed profile, starting from 130 km/h, and separately generated left and right ISO 8608 Class B profiles are imported as road inputs.

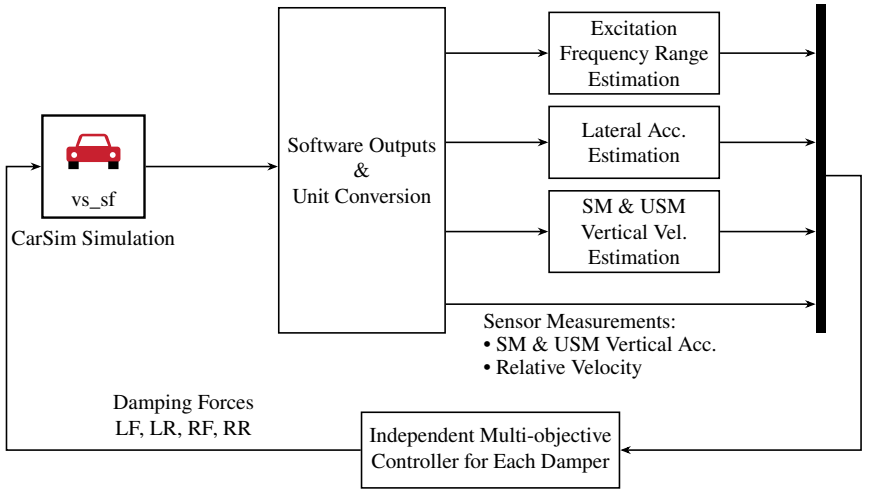


Fig. 12. Schematic representation of the Simulink and CarSim joint simulation

The first test is the ISO 3888-2 Double Lane Change (DLC), a highly transient maneuver that assesses handling and stability during rapid obstacle avoidance (Figure 13).

As shown in Figure 14(a), the controller prioritizes the comfort objective during the initial 18 meters, corresponding to straight-line driving. Once the avoidance maneuver begins, it switches to handling-oriented control. When the vehicle returns to its original lane at approximately the 77th meter and the lateral acceleration stabilizes below the threshold, the controller reverts to comfort mode.

Figure 14(b) shows the road-tracking benefit: under sharply steered conditions the passive vehicle slips laterally between the 20th and 80th meters, degrading path-following, whereas the proposed controller markedly reduces this slip, enhancing

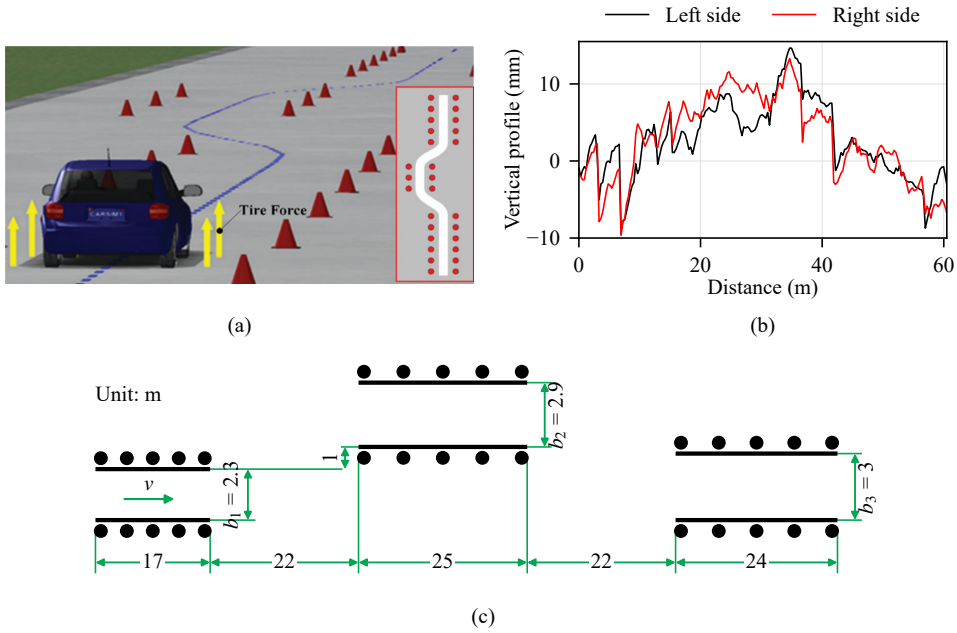


Fig. 13. Double Lane Change (DLC) test scenario

handling and safety. Relative to the passive suspension, the RMS lateral deviation from the driver target path is reduced from 0.51 m to 0.29 m, a reduction of 44%, and the maximum deviation from 1.42 m to 0.73 m, a reduction of 48%.

In Figure 14(c), the ability of the proposed controller to minimize vertical tire force variation is clearly observed. Over the 20–80 m maneuver region, the RMS dynamic tire load is reduced by 13% and its peak value by 48% relative to the passive suspension, whereas over the remainder of the run, where comfort is prioritized, the RMS dynamic tire load is 63% higher. In exchange, the ISO 2631 frequency-weighted RMS sprung-mass acceleration on these segments is 18% and 25% lower. In the passive suspension case, the front-left tire loses contact with the road twice, at approximately $t = 2.5$ s and $t = 5.5$ s. However, with the proposed controller, tire–road contact is maintained throughout the entire test. This figure also illustrates the adaptive switching behavior of the controller: during the intervals $t_{\text{interval},1} = 0$–$1.5$ s and $t_{\text{interval},2} = 6.5$–$8$ s, the controller operates in comfort mode, resulting in higher vertical tire force variation than the passive case. Nonetheless, as these periods correspond to straight-line motion, passenger comfort takes precedence over handling, justifying the controller's prioritization strategy.

The second test is a high-speed racetrack scenario evaluating handling, ride comfort, and path-following together. The closed-loop track combines straight and curved segments (Figure 15(b)), spans 2500 m, and has the elevation profile of Figure 15(d).

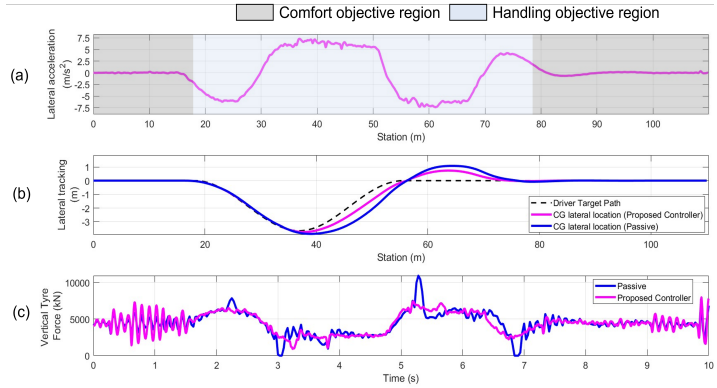


Fig. 14. Performance of the control algorithm in DLC test

For simplicity, a one-dimensional road-roughness model represents the tire-ground contact instead of a full 3D surface: ISO Class B random roughness over the entire 2500 m, with independent left and right tracks (Figure 15(c)).

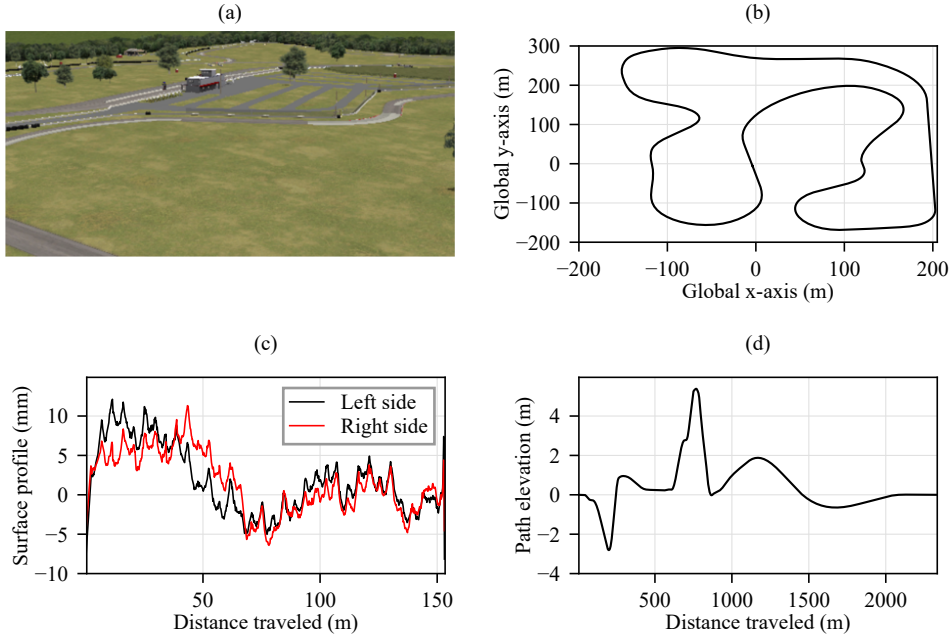


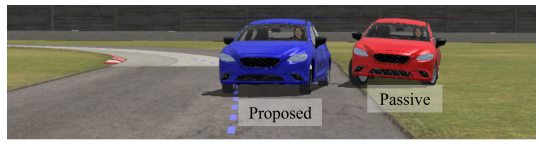
Fig. 15. High speed race track test (a) general view (b) track profile in horizontal plane (c) B class surface roughness (d) path elevation

Figures 16 and 17 illustrate the performance of the proposed control algorithm. As can be seen in Figure 16(a), in the sharp curve around the 150-meter mark, the vehicle equipped with passive suspension fails to maintain its trajectory and exits

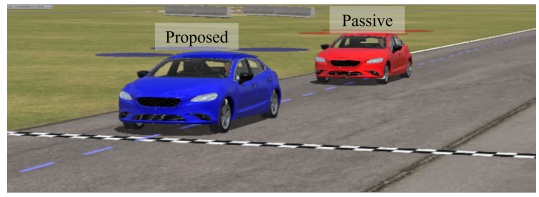
the lane. In contrast, the vehicle using the proposed controller maintains better tire–road contact, enabling greater lateral cornering force and thus maintaining the road track. This results in improved handling stability, which is a critical requirement in high-speed dynamic maneuvers.

As shown in Figure 16(b), the vehicle with the proposed controller completes the lap about 13 m (0.44 s) ahead of its passive counterpart. Both vehicles use the same powertrain, tires, driver model, and target speed profile. Most of this lead is gained between 1380 and 1560 m, where the proposed controller keeps the vehicle on the race line (Figure 17(a)) and the driver model can carry up to 6.4 km/h more speed through the corner. In the lateral tracking analysis between the 1400th and 1500th meters of the track (Figure 17a), the proposed controller reduces lateral path deviation by 2.5 meters compared to the passive configuration. Additionally, the proposed system maintains lower vertical tire force variation throughout the test. While the passive system's right front tire loses ground contact 12 times, this number is reduced to only 2 instances under the proposed control, as can be seen in Figure 17(b).

Figure 17(c) further confirms the ride comfort advantage of the proposed strategy, with a 41% reduction in the RMS value of heave acceleration compared to the passive suspension. Evaluated according to ISO 2631-1, with the W_k filter of Annex A band-limited at 0.4 Hz and the RMS taken over the full run at the 40 Hz output rate of the passive simulation (band limit 20 Hz), the weighted RMS falls from 0.092 to 0.039 m/s^2, a reduction of 57%. Since the crest factor exceeds 9, the vibration dose value is also given; it falls from 0.62 to 0.26 m/s$^{1.75}$. Figure 17(d) shows that the reduction grows from 36% below 4 Hz to 87% above 8 Hz, where W_k is close to unity. The combination of improved handling stability, reduced tracking error, enhanced tire contact, and superior ride comfort supports the effectiveness of the multi-objective controller across a range of driving scenarios, as evidenced in both Scenario 1 and Scenario 2.



(a)



(b)

Fig. 16. Important instants from the race track simulation

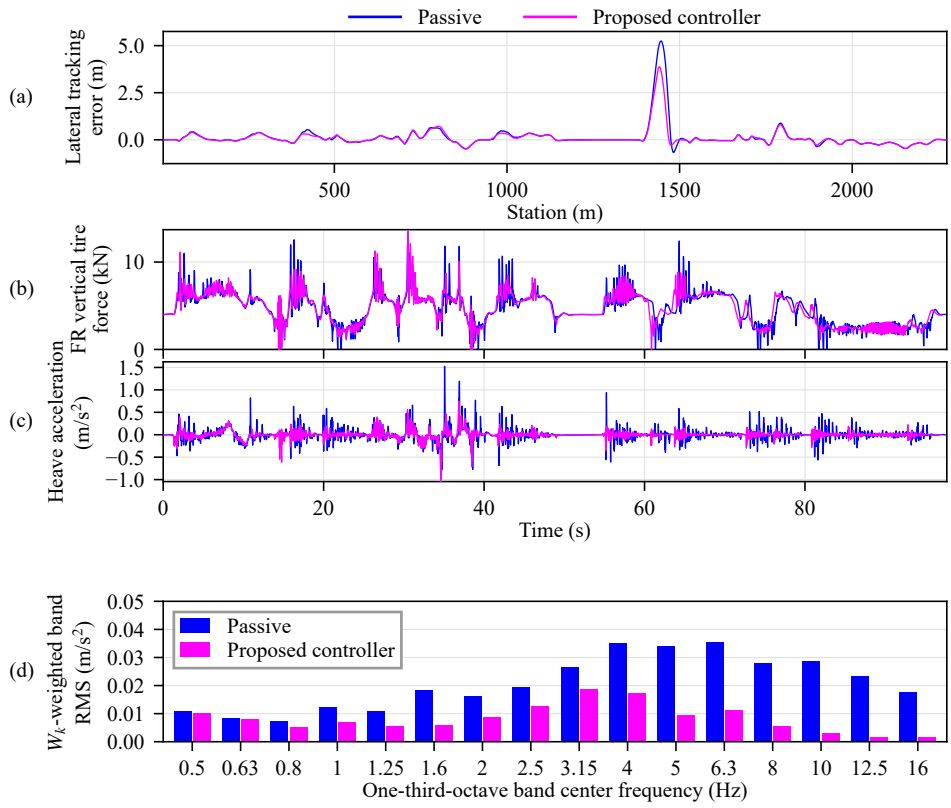


Fig. 17. Performance of the proposed controller in race track simulation; (d) one-third-octave spectrum of the W_k-weighted heave acceleration

7. Conclusions

This study presents the development and validation of a heuristic multi-objective control algorithm for semi-active suspension systems, in the supervisory-arbitration sense defined in Sec. 1 and Sec. 6. The proposed control architecture dynamically balances comfort and handling objectives by adapting to instantaneous road excitation characteristics and driving conditions. Unlike fixed-weight hybrid SH-GH schemes, the controller adapts along two axes: it responds effectively across a wide range of road excitation frequencies and transitions between comfort- and handling-oriented control based on real-time lateral acceleration data. Furthermore, the algorithm proposes an adaptive cross-over frequency update mechanism to accommodate variations in tire pressure and cabin loading conditions.

A novel FFT-based state variable estimation method was proposed to overcome practical challenges associated with measuring absolute and relative velocities, enabling real-time implementation without the need for costly or impractical sensor configurations.

Quantitatively, relative to the passive suspension the proposed strategy reduced the tire deflection by 38% (RMS) and 31% (MaxAE) under 1.5 Hz sinusoidal excitation, reduced the RMS tire deflection by 34.7% under an ISO-8608 Class D random profile, estimated the sprung-mass velocity in real time with a maximum absolute error of 0.0056 m/s, and, in the high-speed racetrack scenario, cut the RMS heave acceleration by 41%, and its ISO 2631-1 weighted value by 57%, while reducing front-tire ground-contact losses from twelve instances to two. Taken together, these figures confirm consistent gains in lateral stability, ride comfort, and trajectory tracking.

The present study has four main limitations. First, the validation is by simulation only: the control laws were developed on a quarter-car model and tested in CarSim–Simulink co-simulation, with the damper represented by a linear coefficient without force saturation or thermal effects, and with the sensor imperfections of Sec. 5.3 applied synthetically. Second, switching is hard: the supervisor uses a single threshold without hysteresis. Third, the estimator has a 7.8 ms refresh interval, and no estimate is available during the first 4 s. Fourth, the cross-over frequency maps are computed offline for a specific vehicle and refreshed once per key cycle, so changes in tire stiffness with temperature and in-cabin load during a trip are not captured.

A formal Pareto-based multi-objective optimization, a sensitivity study of the estimator latency under sharp transient events, and the addition of a hysteresis or blending buffer to suppress switching chatter are left as future work, alongside experimental validation on a physical test platform. A quantitative benchmarking of the proposed architecture against fixed-weight hybrid SH-GH control, with both implemented in the same full-vehicle environment and evaluated under identical maneuvers, is also left to a dedicated study. In addition, the cross-over frequencies are refreshed once per key cycle, so in-trip variation of tire stiffness with tire temperature, and of cabin load at intermediate stops, is not captured; fully continuous online adaptation of the cross-over frequencies remains a future refinement.

Author contributions

The authors confirm contribution to the paper as follows: study conception and design: Jifu Guan, Ali Caglar Sonmez; data collection: Ali Caglar Sonmez; analysis and interpretation of results: Jifu Guan, Ali Caglar Sonmez; draft manuscript preparation: Ali Caglar Sonmez. All authors reviewed the results and approved the final version of the manuscript.

References

[1] A.M.A. Soliman and M.M.S. Kaldas. Semi-active suspension systems from research to mass-market–a review. *Journal of Low Frequency Noise, Vibration and Active Control*, 40(2): 1005–1023, 2021. doi: 10.1177/1461348419876392.

[2] J.C. Tudon-Martinez, R. Morales-Menendez, R.A. Ramirez-Mendoza, and L. Amezquita-Brooks. Comparison of heuristic controllers for an automotive semi-active suspension. *IFAC Proceedings Volumes*, 47(3):6307–6312, 2014. doi: 10.3182/20140824-6-ZA-1003.01835.

[3] S. Kurczyk and M. Pawełczyk. Fuzzy control for semi-active vehicle suspension. *Journal of Low Frequency Noise, Vibration and Active Control*, 32(3):217–225, 2013. doi: 10.1260/0263-0923.32.3.217.

[4] M.-Q. Nguyen, M. Canale, O. Sename, and L. Dugard. A model predictive control approach for semi-active suspension control problem of a full car. In *2016 IEEE 55th Conference on Decision and Control (CDC)*, pages 721–726. IEEE, 2016. doi: 10.1109/CDC.2016.7798353.

[5] M. Ghoniem, T. Awad, and O. Mokhiamar. Control of a new low-cost semi-active vehicle suspension system using artificial neural networks. *Alexandria Engineering Journal*, 59(5): 4013–4025, 2020. doi: 10.1016/j.aej.2020.07.007.

[6] D. Karnopp. Active damping in road vehicle suspension systems. *Vehicle System Dynamics*, 12(6):291–311, 1983. doi: 10.1080/00423118308968758.

[7] S.M. Savaresi, E. Silani, and S. Bittanti. Acceleration-driven-damper (ADD): an optimal control algorithm for comfort-oriented semiactive suspensions. *Journal of Dynamic Systems, Measurement, and Control*, 127(2):218–229, 2005. doi: 10.1115/1.1898241.

[8] S.M. Savaresi and C. Spelta. Mixed sky-hook and ADD: Approaching the filtering limits of a semi-active suspension. *Journal of Dynamic Systems, Measurement, and Control*, 129(4): 382–392, 2007. doi: 10.1115/1.2745846.

[9] M. Valášek, M. Novak, Z. Šika, and O. Vaculin. Extended ground-hook-new concept of semi-active control of truck's suspension. *Vehicle System Dynamics*, 27(5-6):289–303, 1997. doi: 10.1080/00423119708969333.

[10] S. Kopylov, Z.B. Chen, and M.A.A. Abdelkareem. Acceleration based ground-hook control of an electromagnetic regenerative tuned mass damper for automotive application. *Alexandria Engineering Journal*, 59(6):4933–4946, 2020. doi: 10.1016/j.aej.2020.09.010.

[11] V. Sankaranarayanan, M.E. Emekli, B.A. Gilvenc, L. Guvenc, E.S. Ozturk, E.S. Ersolmaz, I.E. Eyol, and M. Sinal. Semiactive suspension control of a light commercial vehicle. *IEEE/ASME Transactions On Mechatronics*, 13(5):598–604, 2008. doi: 10.1109/TMECH.2008.2001397.

[12] B.-C. Chen, Y.-H. Shiu, and F.-C. Hsieh. Sliding-mode control for semi-active suspension with actuator dynamics. *Vehicle System Dynamics*, 49(1-2):277–290, 2011. doi: 10.1080/00423111003602376.

[13] L.H. Nguyen, K.-S. Hong, and S. Park. Road-frequency adaptive control for semi-active suspension systems. *International Journal of Control, Automation and Systems*, 8(5):1029–1038, 2010. doi: 10.1007/s12555-010-0512-1.

[14] M. Gu and Z. Lyu. Identification of a mechanism's vibration velocity and displacement based on the acceleration measurement. *Mechanical Science and Technology for Aerospace Engineering*, 30(4):522–526, 2011.

[15] D. Sammier, O. Sename, and L. Dugard. Skyhook and h_∞ control of semi-active suspensions: some practical aspects. *Vehicle System Dynamics*, 39(4):279–308, 2003. doi: 10.1076/vesd.39.4.279.14149.

[16] J.H. Crews, M.G. Mattson, and G.D. Buckner. Multi-objective control optimization for semi-active vehicle suspensions. *Journal of Sound and Vibration*, 330(23):5502–5516, 2011. doi: 10.1016/j.jsv.2011.05.036.

[17] M. Gobbi, F. Levi, and G. Mastinu. Multi-objective stochastic optimisation of the suspension system of road vehicles. *Journal of Sound and Vibration*, 298(4-5):1055–1072, 2006. doi: 10.1016/j.jsv.2006.06.041.

[18] A. Jamali, H. Shams, and M. Fasihozaman. Pareto multi-objective optimum design of vehicle-suspension system under random road excitations. *Proceedings of the Institution of Mechanical Engineers, Part K: Journal of Multi-body Dynamics*, 228(3):282–293, 2014. doi: 10.1177/1464419314531757.

[19] M. Momen, S. Ebrahimi-Nejad, and M. Mollajafari. Multi-objective optimization of exponential-cross-section piezoelectric cantilever under tire rotational excitation for self-powered tire pressure monitoring systems. *Journal of Cleaner Production*, 500:145255, 2025. doi: 10.1016/j.jclepro.2025.145255.

[20] M. Mollajafari and M.H. Shojaeefard. TC3PoP: a time-cost compromised workflow scheduling heuristic customized for cloud environments. *Cluster Computing*, 24(3):2639–2656, 2021. doi: 10.1007/s10586-021-03285-5.

[21] M. Shojaeefard, M. Mollajafari, S. Mousavitabar, M. Khordehbinan, and H. Hosseinalibeiki. A TSP-based nested clustering approach to solve multi-depot heterogeneous fleet routing problem. *Revista Internacional de Métodos Numéricos para Cálculo y Diseño en Ingeniería*, 38(1):1–11, 2022. doi: 10.23967/j.rimni.2022.03.001.

[22] P.G. Pashakolaee, H.S. Shahhoseini, and M. Mollajafari. Hyper-chaotic feeded GA (HFGA): a reversible optimization technique for robust and sensitive image encryption. *Multimedia Tools and Applications*, 77(16):20385–20414, 2018. doi: 10.1007/s11042-017-5461-8.

[23] S. Nazemi, M.M. Tehrani, and M. Mollajafari. GA tuned h_∞ roll acceleration controller based on series active variable geometry suspension on rough roads. *International Journal of Vehicle Performance*, 8(2/3):166, 2022. doi: 10.1504/IJVP.2022.122047.

[24] P. Sanaie and M. Mollajafari. Designing a disturbance estimator for electric power steering robust controller. *Mechanical Engineering for Society and Industry*, 4(2):263–276, 2024. doi: 10.31603/mesi.12650.

[25] S.M. Mohtavipour, T.Z. Ehsan, H.J. Abeshoori, and M. Mollajafari. Smooth longitudinal driving strategy with adjustable nonlinear reference model for autonomous vehicles. *International Journal of Dynamics and Control*, 11(5):2320–2334, 2023. doi: 10.1007/s40435-023-01142-4.

[26] M.H. Shojaeifard, M. Mollajafari, M. Talebi, and M. Naserian. A novel finite-time leader-follower consensus control for a disturbed mechanical nonlinear system in presence of actuator saturation. *Automatika*, 65(3):1191–1200, 2024. doi: 10.1080/00051144.2024.2329493.

[27] H. Hassanpour, S. Ebrahimi-Nejad, and M. Mollajafari. Parametric study of permanent magnet eddy current brake considering demagnetization, temperature, edge, and skin effects: Numerical and experimental investigation. *Applications in Engineering Science*, 22:100235, 2025. doi: 10.1016/j.apples.2025.100235.

[28] M. Raeesi, P. Chavoshnia, S. Mansouri, and M. Mollajafari. Beyond energy efficiency: A battery-aware reward design for deep reinforcement learning-based energy management in electric vehicles with hybrid storage. *Journal of Energy Storage*, 176:123376, 2026. doi: 10.1016/j.est.2026.123376.

[29] M. Ravanbod, S. Ebrahimi-Nejad, M. Mollajafari, and B. SalehiRad. Porous liner coated inlet duct: a novel approach to attenuate automotive turbocharger inlet flow-induced sound propagation. *Engineering Research Express*, 5(1):015047, 2023. doi: 10.1088/2631-8695/acbfa4.

[30] W. Xu, H. Han, Q. Li, M. Mollajafari, and F. Scott. Layerwise formulation of poroelastic composite plate under pre-buckling and thermal shock loading. *Composite Structures*, 304: 116343, 2023. doi: 10.1016/j.compstruct.2022.116343.

[31] F.D. Goncalves and M. Ahmadian. A hybrid control policy for semi-active vehicle suspensions. *Shock and Vibration*, 10(1):59–69, 2003. doi: 10.1155/2003/897173.

[32] M. Ahmadian and C.A. Pare. A quarter-car experimental analysis of alternative semiactive control methods. *Journal of Intelligent Material Systems and Structures*, 11(8):604–612, 2000. doi: 10.1177/104538900772663973.

[33] A. Ranjan, S. Prasanth, F. Cherian, J.P. Bhasker, and K. Ravi. Adaptive hybrid control strategy for semi-active suspension system. In *IOP Conference Series: Materials Science and Engineering*, volume 263, page 062062. IOP Publishing, 2017. doi: 10.1088/1757-899X/263/6/062062.

[34] W. Wang and J. Xi. Study of semi-active suspension control strategy based on driving behaviour characteristics. *International Journal of Vehicle Design*, 68(1-3):141–161, 2015. doi: 10.1504/IJVD.2015.071070.

[35] M. Corno, O. Galluppi, G. Panzani, A. Sinigaglia, P. Capuano, J. Cecconi, and S.M. Savaresi. Design and validation of a full body control semi-active suspension strategy for a supercar. *IFAC-PapersOnLine*, 52(5):667–672, 2019. doi: 10.1016/j.ifacol.2019.09.106.

[36] A.D. Damavandi, B. Mashadi, and M. Masih-Tehrani. Development of a hybrid intelligent switching hydraulically interconnected suspension system under a multi-objective optimized mode selection strategy with real-world condition. *Proceedings of the Institution of Mechanical Engineers, Part D: Journal of Automobile Engineering*, 239(4):1222–1239, 2024. doi: 10.1177/09544070231217558.

[37] H. Gheibollahi and M. Masih-Tehrani. A multi-objective optimization method based on NSGA-II algorithm and entropy weighted TOPSIS for fuzzy active seat suspension of articulated truck semi-trailer. *Proceedings of the Institution of Mechanical Engineers, Part C: Journal of Mechanical Engineering Science*, 237(17):3809–3826, 2023. doi: 10.1177/09544062231151799.

[38] R. Rajamani. *Vehicle dynamics and control*. Springer, 2011. doi: 10.1007/978-1-4614-1433-9.

[39] R. Pintelon and J. Schoukens. *System Identification: A Frequency Domain Approach*. John Wiley & Sons, 2012. doi: 10.1002/9781118287422.

[40] Y. Deng, Z. Wang, H. Shen, J. Gong, and Z. Xiao. A comprehensive review on non-pneumatic tyre research. *Materials & Design*, 227:111742, 2023. doi: 10.1016/j.matdes.2023.111742.

[41] U. Kiencke and L. Nielsen. *Automotive control systems: for engine, driveline, and vehicle*. Springer, Berlin, Heidelberg, 2000.